Supporting Information

for

Nonlinear Geometric Phase Control via High-Q Quasi-BIC Resonance in All-Dielectric Metasurfaces

He-Rui Yang,[ac] Wen-Juan Shi,[a] Cong-Fu Zhang,[ac] Wang-Hao Zhu,[ac] Di Ma,[ac] Shao-Jie Li,[ac] Zhao-Lu Wang[a] and Hong-Jun Liu[ab*]

a. State Key Laboratory of Ultrafast Optical Science and Technology, Xi'an Institute of Optics and Precision Mechanics, Chinese Academy of Sciences, Xi'an 710119, China.

b. Collaborative Innovation Center of Extreme Optics, Shanxi University, Taiyuan 030006, China.

c. University of Chinese Academy of Sciences, Beijing 100084, China.

Corresponding author E-mail: liuhongjun@opt.ac.cn.

1.Simulation Methods

To calculate the transmission phase and third-harmonic conversion efficiency of the silicon nanoresonator array, full-wave simulations were performed in the frequency domain using the finite element method (FEM) implemented in COMSOL Multiphysics. Periodic boundary conditions were applied in the x–y plane, and perfectly matched layers (PMLs) were set along the z-direction to eliminate reflections.First, the spatial distribution of the fundamental electromagnetic field was computed. The third-harmonic field in free space was then obtained from the nonlinear polarization defined by the total fundamental field as: $P_{NL}^{(3)}(\mathbf{r},3\omega) = \varepsilon_0 \chi^{(3)} \vdots EEE$. In the simulation, amorphous silicon was modeled as an isotropic medium with third-order susceptibility parameters of $\chi_{iiii}^{(3)} = 2.45\times10^{-19} m^2/V^2$,[1,2] $\chi_{ijjj}^{(3)} = \chi_{ijij}^{(3)} = \chi_{ijji}^{(3)} = \frac{1}{3}\chi_{iiii}^{(3)}$ where i, j correspond to the x, y, z coordinates. The complex refractive index of amorphous silicon was taken from the experimental data of Pierce and Spicer (1972), while the refractive index of the quartz substrate was fixed at n = 1.45.

2.Analytical Methods utilized to calculate mode properties

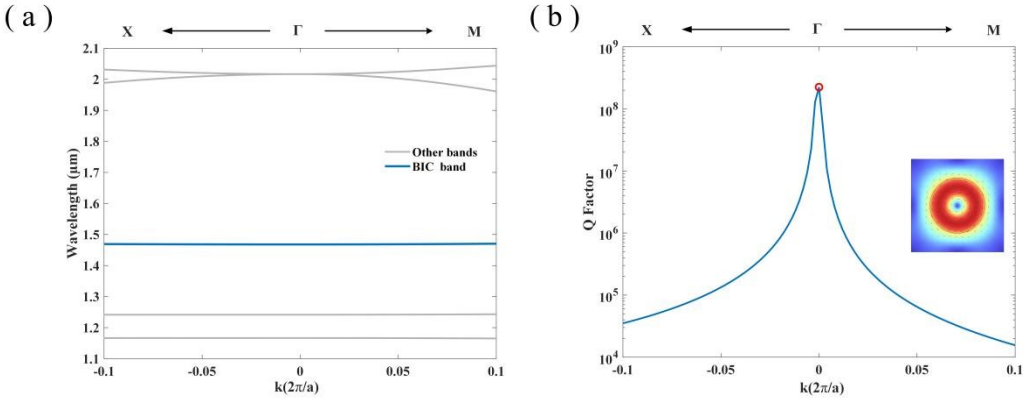

Figure S1. Analysis of the resonant mode in the symmetric structure. (a) The calculated band structure for the symmetric unit cell is presented. This reveals the dispersion relationship of the supported electromagnetic modes; (b) To further characterize the resonance, the quality (Q) factor of the mode is plotted as a function of the wave vector. The inset provides essential visual context, displaying both a schematic of the unit cell and the corresponding electric field distribution of the mode in the XY plane.

For the unperturbed structure (r=0), the band structure was calculated using the eigenfrequency solver in COMSOL Multiphysics. As depicted in Figure S1(a), multiple resonant modes are present in the near-infrared spectral range. Among these modes, we focus on the one highlighted by the blue curve. Its quality (Q) factor was numerically calculated using the formula Q = Re(ω) / [2Im(ω)], where ω represents the complex angular frequency of the eigenmode. The calculated Q factor is plotted as a function of the wave vector in Figure S1(b). Notably, the Q factor increases

exponentially as the wave vector approaches the Γ point (k=0), reaching a theoretical maximum exceeding 10^8. This divergence is a clear signature of a symmetry-protected BIC at the center of the Brillouin zone.

3.Linear Geometric Phase Response

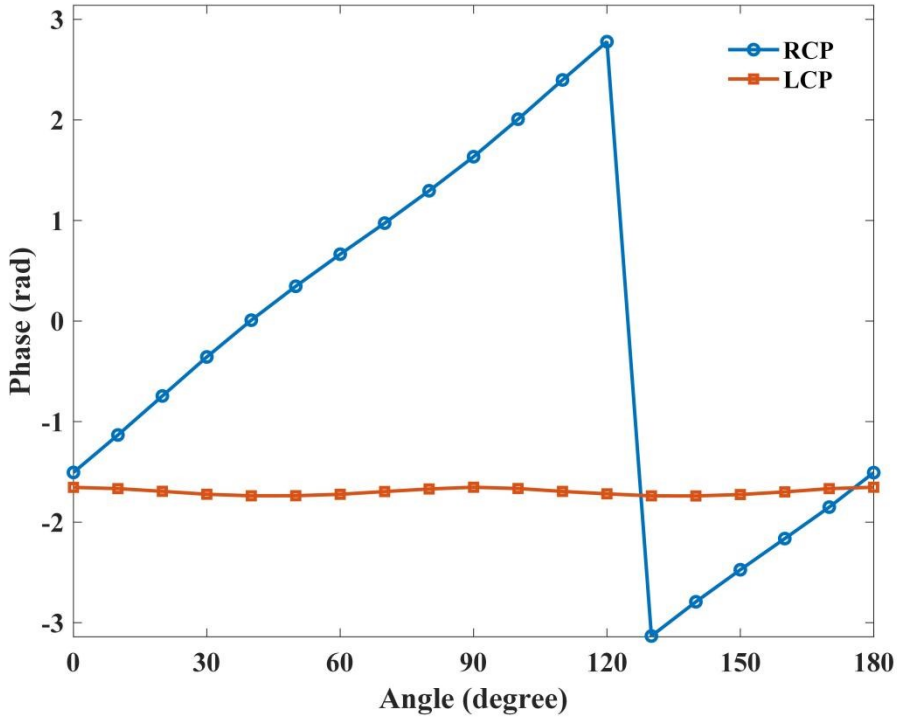

Figure S2. The simulated linear geometric phase is plotted for both co-polarized and cross-polarized components as the silicon resonator unit is rotated from 0° to 180° in 5° increments. This demonstrates the phase modulation capability of the unit.

4.Fabrication Tolerance Analysis

1. Analysis of Key Fabrication Error Sources

Based on the proposed structure (a silicon pillar with an eccentric air hole), the primary sources of fabrication errors and their typical ranges are summarized as follows:

Table1.The primary sources of fabrication errors and their typical ranges based on the proposed structure.

Structural parameter	Typical error source	Estimated error range
Lattice period (P)	Lithography alignment error	±10 nm
Pillar height (H)	Etching depth control	±20 nm
Pillar radius (R)	Sidewall etching slope	±10 nm
Air-hole radius (r)	Etching process variation	±5 nm
Air-hole offset (l)	E-beam lithography positioning error	±10 nm

2. Sensitivity to Fabrication Errors

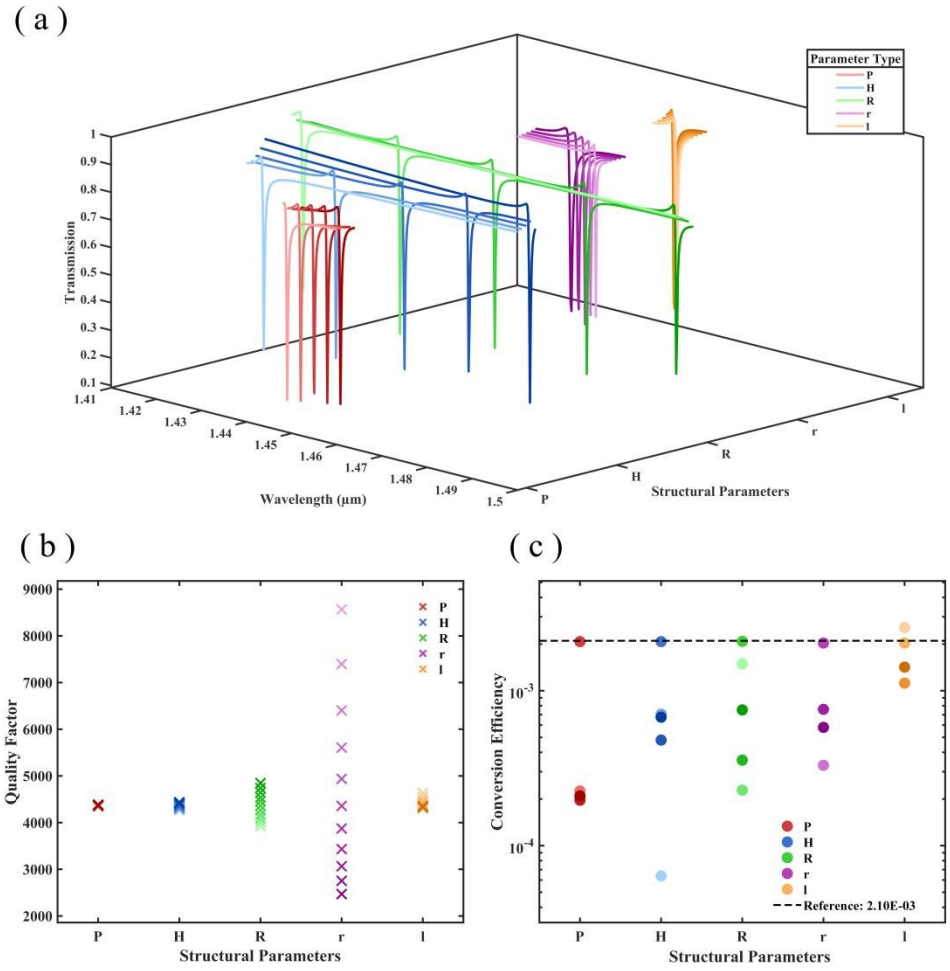

Figure S3 illustrates the variations in the transmission spectra, quality factors , and THG conversion efficiency as different structural parameters are tuned.

As shown in Fig. S3(a), we fix all other parameters and vary the lattice period P from 730nm to 750nm with a step of 10nm, where the color gradually changes from light to dark red to indicate increasing P. During this process, the overall shape of the transmission spectra remains largely unchanged, while the resonance peak exhibits a clear redshift. Similarly, the silicon pillar height H is varied from 190nm to 230nm in steps of 10nm (indicated by a light-to-dark blue color gradient), and the pillar radius R is varied from 210nm to 230nm in steps of 5nm (with increasing color depth). In both cases, increasing the parameter leads to redshift of the resonance wavelength. In

contrast, when the air-hole radius r is increased from 25nm to 35nm in steps of 2.5nm, or when the offset l is increased from 80nm to 100nm in steps of 5nm, the resonance peak exhibits blueshift. A comparative analysis indicates that the silicon pillar radius R and height H have a more pronounced influence on the resonance position. Figure S3(b) presents the dependence of the Q-factor on individual structural parameters (P,H,R,r,l), with all other parameters fixed. It can be observed that variations in P,H, and R within the considered ranges have a limited impact on the Q-factor, whereas changes in r significantly affect the Q-factor. This behavior is consistent with the symmetry-breaking nature of QBICs, where a smaller asymmetry parameter generally leads to a higher Q-factor. Although l is also an asymmetry parameter, its influence on the Q-factor appears weaker because the considered values of l are relatively large. This interpretation is further supported by the analysis in manuscript Fig. 3(c). Figure S3(b) illustrates the variation of THG efficiency as each structural parameter is varied individually while keeping the others fixed. The black dashed lines indicate the final selected parameter set. Overall, these results demonstrate that the chosen parameters represent a carefully optimized solution. It is important to emphasize that our goal is not simply to maximize the Q-factor or THG efficiency. Instead, we seek a parameter regime that simultaneously supports continuous and linear nonlinear geometric-phase modulation at the THG wavelength. During the optimization process, we found that some parameter combinations yield extremely high conversion efficiencies but fail to provide good phase linearity, and therefore do not meet our design objectives. Consequently, the selected resonance wavelength reflects a balanced consideration of nonlinear geometric-phase control and conversion efficiency. This also explains why, although the resonance wavelength and Q-factor vary monotonically with structural parameters in Figs. S3(a) and (b), the THG efficiency does not follow the same trend.

Table2.THG Efficiency Range based on the proposed structure and their typical ranges.

Structure Parameter	Maximum Value /nm	Minimum Value /nm	THG Efficiency Range
Lattice period (P)	730.0	750.0	1.96E-4 ~ 2.07E-3
Pillar height (H)	190.0	230.0	6.38E-5 ~ 2.07E-3
Pillar radius (R)	210.0	230.0	2.28E-4 ~ 2.08E-3
Air-hole radius (r)	25.0	35.0	9.12E-5 ~ 2.03E-3
Air-hole offset (l)	85.0	100.0	1.12E-3 ~ 2.55E-3

In summary, while certain parameter combinations can produce higher Q-factors or locally enhanced THG efficiency, they do not necessarily satisfy the requirement of continuous phase tunability. The final parameter set represents a global optimum that balances resonance wavelength, Q-factor, THG efficiency, and—most critically—the linearity of phase modulation. This optimization strategy ensures that the proposed device exhibits not only a strong nonlinear response but also flexible wavefront control capability.

Reference

1. L. Wang, S. Kruk, K. Koshelev, I. Kravchenko, B. L. Davies, and Y. Kivshar, Nonlinear Wavefront Control with All-Dielectric Metasurfaces, Nano Lett., 2018 18 (6), 3978-3984.

2.K. Koshelev, Y. T. Tang, K. F. Li, D. Y. Choi, G. X. Li, and Y. Kivshar, Nonlinear Metasurfaces Governed by Bound States in the Continuum, ACS Photonics, 2019 6 (7), 1639-1644.

3. D. T. Pierce and W. E. Spicer, Electronic structure of amorphous Si from photoemission and optical studies, Phys. Rev. B,1972, 5, 3017–3029.